AGU PUBLICATIONS

JGR

Journal of Geophysical Research: Space Physics

RESEARCH ARTICLE

10.1002/2014JA020473

Key Points:
- Thermospheric waves were excited by flare in the subsolar region
- Gravity waves converged in the antisubsolar region when the flare occurred
- Penetration E fields drive equatorial neutral wave through neutral-ion coupling

Correspondence to:
J. Zhu,
zhjie@umich.edu

Citation:
Zhu, J., and A. J. Ridley (2014), Modeling subsolar thermospheric waves during a solar flare and penetration electric fields, *J. Geophys. Res. Space Physics*, *119*, 10,507–10,527, doi:10.1002/2014JA020473.

Received 5 AUG 2014
Accepted 30 NOV 2014
Accepted article online 3 DEC 2014
Published online 18 DEC 2014

Modeling subsolar thermospheric waves during a solar flare and penetration electric fields

Jie Zhu[1] and Aaron J. Ridley[1]

[1]Department of Atmospheric, Oceanic and Space Sciences, University of Michigan, Ann Arbor, Michigan, USA

Abstract Thermospheric waves occurring around the time of the 14 July 2000 solar flare were investigated using the Global Ionosphere and Thermosphere Model. The simulation results showed that extensive acoustic and gravity waves were excited by the solar flare in the subsolar region. The subsolar buoyancy period at 400 km altitude was approximately 16 min. Gravity waves with frequencies lower than the buoyancy frequency traveled from the dayside to the nightside and converged in the longitudinal region that was the antisubsolar region when the flare occurred. Acoustic waves with frequencies well above the buoyancy frequency propagated upward from approximately 130 km altitude with increasing amplitudes. The power spectra of the vertical neutral winds in the acoustic branch peaked at a period of approximately 13 min, just below the buoyancy period. The gradient in pressure was the driver of the two waves, while the ion drag caused a phase delay between the variations in the pressure gradient and the vertical velocity in the acoustic waves. An anticorrelation in the high-frequency component of the vertical neutral wind exists between the subsolar and antisubsolar points at times away from the flare, which was driven by the rapid variations of the ion flows due to the penetration electric field. It is suggested that the penetration of the high-latitude interplanetary magnetic field electric field to low latitudes can drive neutral waves in the equatorial region through momentum coupling with rapidly changing ion flows.

1. Introduction

The ionospheric response to solar flares and penetration electric fields have been widely studied for decades [*Garriott et al.*, 1967; *Davides*, 1990]. A solar flare is a sudden enhancement in solar emissions in the X-ray and extreme ultraviolet (EUV) wavelengths. These emissions can cause a rapid increase in the total electron content (TEC) on the dayside of the ionosphere [*Mendillo et al.*, 1974] and may also result in sudden ionospheric disturbances [*Donnelly*, 1967; *Jones*, 1971; *Stonehocker*, 1970]. The recent use of the global positioning system network in mapping TEC [*Coster and Komjathy*, 2008; *Rideout and Coster*, 2006] has further improved the understanding of the ionospheric response to solar flares. Compared to the extensive studies of the ionospheric response to these rapid variations, the thermospheric response has received less attention. This is partly because the dense neutral atmosphere was expected to react sluggishly to such short time scale phenomena. However, observations by Challenging Minisatellite Payload show rapid increases in the neutral density within a few minutes of the flare onset [*Liu et al.*, 2007]. Day-to-night propagating gravity waves, launched by dayside heating during a solar flare, were simulated by a model [*Pawlowski and Ridley*, 2008], but there have been very few studies that have shown whether other neutral waves are generated by solar flares and, if so, what their characteristics may be.

Penetration electric fields are another rapid driver of the ionosphere. Two primary electric fields exist in the low- and middle-latitude ionosphere: the wind dynamo electric field and the penetration electric field. The neutral wind dynamo is the interaction between the neutral winds and the electrically conducting ionosphere to generate electric fields and currents [*Kato*, 1956, 1957; *Tarpley*, 1970, *Richmond*, 1989]. Penetration electric fields from high latitudes down to low latitudes have two primary sources: the interplanetary electric field and the electric field perturbations associated with substorms [*Kikuchi et al.*, 2000; *Sastri et al.*, 2001]. The penetration of the dayside high-latitude electric field, caused by direct connection between the magnetosphere and the interplanetary magnetic field, to low latitudes was first suggested by *Nishida* [1968] and has been extensively studied using the incoherent scatter radars [*Kelley et al.*, 1979; *Fejer et al.*, 1979; *Huang and Foster*, 2005]. The electric field is confined in the high latitudes by the shielding effect of the region 2 field-aligned currents [*Vasyliunas*, 1972]. However, the slow response of the region 2 currents to the rapid changes in the region 1 currents caused by variations in the interplanetary

magnetic field (IMF) cannot effectively cancel out the primary high-latitude electric field, resulting in the penetration of electric fields to low latitudes [*Vasyliunas*, 1972; *Southwood*, 1977]. The equatorial E × B drift caused by the penetration of the high-latitude electric field during storm time has been simulated by models, and the comparison of the vertical ion drifts between model and observation at the magnetic equator has been investigated [*Maruyama et al.*, 2008; *Wang et al.*, 2008]. Although the ionospheric response to the penetration electric field has been established, the influence of the penetration electric field on the neutral wind has not received as much attention.

If the effects of viscosity and coriolis force are ignored, rapid changes in the thermosphere have the ability to drive two types of wave structures, acoustic waves and gravity waves [*Gossard and Hooke*, 1975; *Yeh and Liu*, 1974]. The presence of gravity gives rise to a restoring force known as the buoyancy force, which is responsible for the characteristic oscillations at the buoyancy (Brunt-*Väisälä*) frequency [*Väisälä*, 1925; *Brunt*, 1927]. In a barometric atmosphere where the pressure (or density) of the air changes with altitude [*Kundu and Cohen*, 2008], the buoyancy (angular) frequency N is defined as follows:

$$N = \sqrt{-\frac{g}{\rho_0}\frac{\mathrm{d}\bar{\rho}}{\mathrm{d}z}}, \tag{1}$$

where g is the acceleration due to gravity, ρ_0 is the neutral density at a reference altitude, and $\bar{\rho}$ is the neutral density in hydrostatic balance. When the pressure (or density) exponentially decreases with altitude, the buoyancy frequency can be further written as follows:

$$N = \sqrt{\frac{(\gamma-1)g^2}{{a_s}^2}}, \tag{2}$$

where γ is the adiabatic index and a_s is the local sound speed [*Gombosi*, 1998]. The local sound speed is given by

$$a_s = \sqrt{\frac{\gamma p_0}{\rho_0}}, \tag{3}$$

where p_0 and ρ_0 are the background pressure and density. Two branches of propagational waves exist in the acoustic-gravity waves. The low-frequency branch in the region where $\omega < \omega_1$ is the gravity wave branch. Here ω is the angular frequency of the waves and $\omega_1 = N\sin\theta$, where θ is the propagation angle with respect to the vertical direction. The high-frequency branch is the acoustic wave branch where $\omega > \omega_2$. ω_2 is known as the acoustic cutoff frequency and is given by [*Gombosi*, 1998]

$$\omega_2 = N\sqrt{\frac{\gamma^2}{4(\gamma-1)}}. \tag{4}$$

This cutoff frequency is found to be $1.1N$ assuming γ =1.4, resulting in a frequency slightly greater than the buoyancy frequency. The region $\omega_1 < \omega < \omega_2$ is the "cutoff" region where no propagational waves exist. In addition to the presence of the cutoff frequency of the acoustic waves, the gravity waves that cannot propagate entirely vertically as transverse waves also contribute to the characteristics of the region. The cutoff zone is highly propagation angle dependent, which changes from $[0, N\sqrt{\frac{\gamma^2}{4(\gamma-1)}}]$ for a vertically propagating wave to $[N, N\sqrt{\frac{\gamma^2}{4(\gamma-1)}}]$ for a horizontally propagating wave.

This study investigated the thermospheric waves around the time of the solar flare on 14 July 2000. The following questions were addressed: (1) Can solar flares and penetration electric fields generate waves in the subsolar thermosphere? (2) How do solar flares and penetration electric fields generate neutral waves? and (3) What are the characteristic of these neutral waves?

2. Model

The Global Ionosphere Thermosphere Model (GITM) was used to investigate the wave activity on 14 July 2000. GITM is a three-dimensional model that couples the ionosphere-thermosphere system in spherical coordinates. The model solves the continuity, momentum and energy equations of ions, and neutrals with realistic source terms. GITM solves a more complete vertical neutral momentum equations than hydrostatic

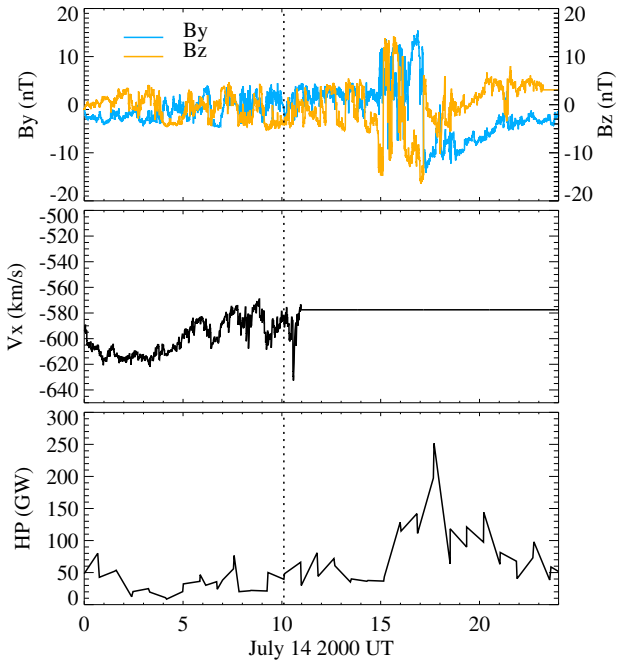

Figure 1. The (top) inteplanetary magnetic field By (blue) and Bz (yellow), (middle) solar wind speed, and the (bottom) Northern Hemispheric power during the flare. The vertical dotted line shows the onset of the flare.

models, allowing it to capture acoustic waves [*Deng et al.*, 2008]. The ion momentum equation is solved in steady state, by taking the pressure gradient, gravity, frictional forces, and electric fields into account [*Ridley et al.*, 2006]. The dynamo electric field is solved for in a self-consistent way by using the technique described by *Richmond* [1995], as described by *Vichare et al.* [2012]. The horizontal grid resolution of the simulations was set to 5° longitude by 2.5° latitude. The International Geomagnetic Reference Field was specified in the simulation. The flare spectrum calculated by the Flare Irradiance Spectral Model (FISM) [*Chamberlin et al.*, 2007] was used as the input for the solar irradiance. FISM is an empirical model that estimates the solar irradiance at wavelengths from 0.1 nm to 190 nm with a 1 nm resolution and time cadence of 60 s [*Chamberlin et al.*, 2007]. The high-latitude electric field was specified by the Weimer potential model [*Weimer*, 2005], which was driven by measured interplanetary magnetic fields (IMFs) and solar wind velocities from the Advanced Composition Explorer (ACE) satellite. The ionospheric potential was updated every 60 s in the simulation, including both the high-latitude and dynamo potentials. In this case, the dynamo boundary was put at 65° magnetic latitude, which allowed a bit of the high-latitude potential to "leak" to the low latitudes. This altered the high-latitude boundary potential on the dynamo, resulting in penetration electric fields.

Figure 1 shows the interplanetary magnetic field and solar wind data measured by the Advanced Composition Explorer (ACE) and the hemispheric power measured by the National Oceanic and Atmospheric Administration (NOAA) satellites. The IMF and solar wind measurements were delayed for an appropriate amount of time using a simple ballistic propagation method [*Ridley*, 2000]. The magnetic field was relatively quiet when the flare occurred at approximately 1003 UT. The IMF then had large rapid variations from approximately 1430 UT–1700 UT, with B_z oscillating between $\pm$ 13 nT. The solar wind velocity data were unavailable shortly after the flare, so a fixed value was used for the remainder of the day.

3. Methodology

This study explored the wave activity in the thermosphere around the time of the X5.7 solar flare on 14 July 2000. The flare event was simulated twice, once accounting for the flare by using the solar irradiance from FISM, and once ignoring the flare by using running 12 h box-medianed FISM data. The simulation with the flare represented the thermospheric response during the flare time and was termed the raw simulation, whereas the difference between the two simulations, with and without the flare, describes only the thermospheric response to the flare under given background conditions and is termed the difference simulation.

Figure 2 shows the solar irradiance at X-ray wavelengths (0.1–0.2 nm) (Figure 2, top) and at extreme ultraviolet (EUV) wavelengths at 58.43 nm (Figure 2, middle) and 97.9 nm (Figure 2, bottom) on 14 July 2000. The yellow lines represent the 12 h medianed irradiances at the corresponding wavelengths. The flare lasted for around 40 min (1003 UT–1043 UT) [*Space Weather Prediction Center*, 2013]. The peak irradiance at 0.1–0.8 nm classifies the flare as an X5.7. The main flare was followed by a small flare (M3.7) that occurred from 1344 UT to 1400 UT. Two EUV wavelengths, 58.43 nm and 97.7 nm, were plotted because of the large photoabsorption and photoionization cross sections for atomic oxygen at 58.43 nm, and for molecular

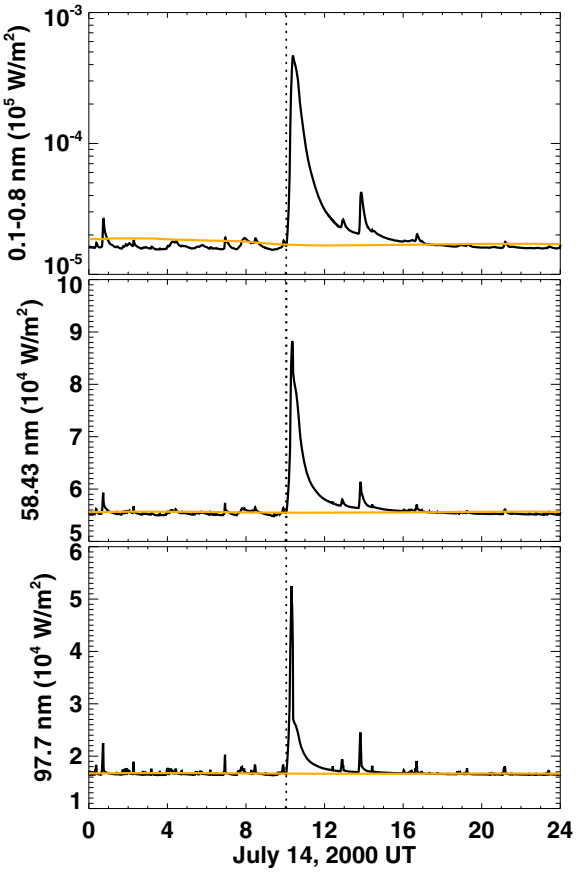

Figure 2. Temporal variations of the solar radiance at X-ray wavelengths (top) (0.1–0.8 nm) and at extreme ultra-violet (EUV) wavelengths: (middle) 58.43 nm and (bottom) 97.7 nm on 14 July 2000. The dashed vertical line at 1003 UT marks the flare onset. Yellow lines represent the 12 h medianed solar irradiances at corresponding wavelengths.

oxygen and nitrogen near 97.7 nm [*Huffman*, 1969]. It was expected that the EUV flux would cause thermospheric responses through photoabsorption of the neutrals and enhanced exothermic chemical reactions due to the increased ionization, as well as through momentum and energy coupling between ions and neutrals.

A fast Fourier transform (FFT) was used to analyze the spectra of the wave activity at the subsolar point at 400 km altitude. The buoyancy frequency was calculated to determine the frequency ranges of acoustic and gravity waves. To examine the temporal evolution of the wave activity, the spectra of the raw and differenced vertical wind using a 2 h moving window were also investigated. The low-frequency component of the neutral dynamics was obtained by taking the mean value of a running 30 min window on the simulation data. The high-frequency component was obtained by subtracting the low-frequency component from the simulation data.

4. Results

4.1. Large-Scale Gravity Waves Initiated by a Solar Flare

Pawlowski and Ridley [2008] found that the intense dayside heating by a solar flare launches nightward propagating gravity waves that transport energy to the nightside at velocities close to the local sound speed plus the bulk neutral wind velocity. This gravity wave that they investigated converged near local midnight after it passed through the dawn and dusk sectors and over both poles, although it was not precisely midnight.

The present study found that this thermospheric disturbance converged at the longitude sector that was midnight when the flare occurred instead of the longitude sector of midnight when the wave arrived approximately 3.5 h later. Figure 3 shows the 5 K isolines from the differenced temperature between the run with and without the flare at 400 km altitude beginning at 1000 UT and ending at 1400 UT on 14 July 2000. The color of the isolines transitions from blue to red with increasing UT. Just after the flare onset at 1030 UT, the initial 5 K isoline appeared, approximately covering the dayside half of the globe. As time progressed, the disturbance gradually traveled toward the nightside and eventually converged at the anti-subsolar point when the flare occurred (thick blue triangle). It took approximately 3.5 h for the disturbance to travel from the dayside and converge at the flare-time midnight. The converging sector was approximately 60° eastward of midnight at the time of convergence (thin blue triangle). One interesting feature was that the isoline at 1345 UT extended a little wider toward the actual midnight, which could possibly be a consequence of the background day-to-night neutral wind pushing the convergence region westward.

Propagation of the global-scale gravity wave caused by the flare was also observed in the vertical neutral wind. The low-frequency component of the vertical neutral winds was obtained by averaging the differenced simulation data with a sliding window of 30 min. This was important since there existed a clear high-frequency component due to acoustic waves, which will be discussed in the subsequent section.

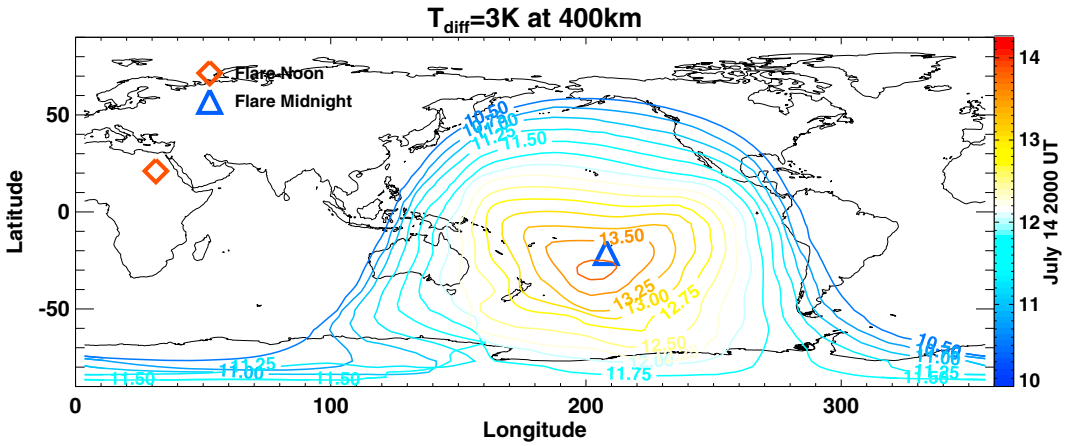

Figure 3. Isolines of the different temperature of 5 K at 400 km altitude from 1000 UT to 1400 UT on 14 July 2000. The colors of the isolines change with the time. The dark diamond and dark triangle represent the subsolar point and antisubsolar point at the flare onset (i.e., 1003 UT). The light triangle marks the antisubsolar point at 1400 UT.

The differenced low-frequency vertical winds caused by the flare are shown in Figure 4. The thick diamond and thick triangle represent the subsolar and antisubsolar sectors when the flare occurred, and the thin diamond and thin triangle mark the locations of the subsolar and antisubsolar regions at the time of the plot. The color scale is saturated at ±0.6 m/s to show the nightside perturbation more clearly. At 0930 UT, prior to the flare onset, the vertical neutral wind was almost unperturbed. At 1030 UT, the flare caused an increase of over 0.6 m/s in the low-frequency vertical neutral wind on the dayside and within the north polar region. The nightside and south polar region were not disturbed by the flare at this time. The difference in the response to the flare between the north and south polar region was attributed to seasonal variation. Because it was summer in the Northern Hemisphere, the South Pole did not receive as much solar irradiance and was not able to respond immediately. At 1130 UT, the dayside perturbation was weakened. Some downward flow existed in the north polar region. At 1230 UT, the low-frequency vertical flow across the entire dayside and north polar region was downward, while the sectors near dawn, dusk, as well as the nightside started showing upward flows. At 1330 UT, downward flow still existed on the dayside and in the north polar region, and the region of upward flow had moved toward the antisubsolar sector at the flare onset (dark triangle) with an increasing amplitude. This indicates that a possible large-scale gravity wave in the vertical neutral wind was excited by the flare as described by *Pawlowski and Ridley* [2008]. This gravity wave traveled from the dayside to the nightside in approximately 3.5 h. Once again, instead of converging on the antisubsolar point at the particular time, the wave converged on the sector that had been the antisubsolar point when the flare onset occurred.

Figure 5 shows the low-frequency component of the differenced vertical winds at the flare-time subsolar (solid line) and antisubsolar (dotted line) points from 0900 UT to 2400 UT. It took approximately 2 h for the gravity waves to start influencing the antisubsolar point. The daytime perturbation had a narrow half "sine" shape with only a very shallow negative phase, while the nighttime perturbation had a wider full sine shape. The antisubsolar wave phase was positive for ~3 h and turned negative around 1600 UT.

4.2. Acoustic Waves Initiated by a Solar Flare

The time period from 0930 UT to 1130 UT was chosen to investigate the acoustic waves around the solar flare on 14 July 2000. Figure 6 shows the temporal variation of the vertical neutral wind at the subsolar sector (moving on the Earth) from 0930 UT to 1130 UT. The dashed vertical line at 1003 UT marks the time of the flare onset. The subsolar location was chosen because it is the most sensitive to changes in solar irradiance, since the solar irradiance directly travels through the atmosphere with no reduction due to the projection to the vertical direction. Figure 6a shows the attitudinal profiles of the raw vertical neutral wind from 100 km to 800 km. The disturbances propagated from lower altitudes to higher altitudes with increasing amplitudes. Because the group velocity of the acoustic waves has the same sign as the phase velocity in all the three directions [*Yeh and Liu*, 1974], the energy was transported upward by the acoustic waves, and in the absence of damping, the amplitude of the wave energy was conserved during the upward

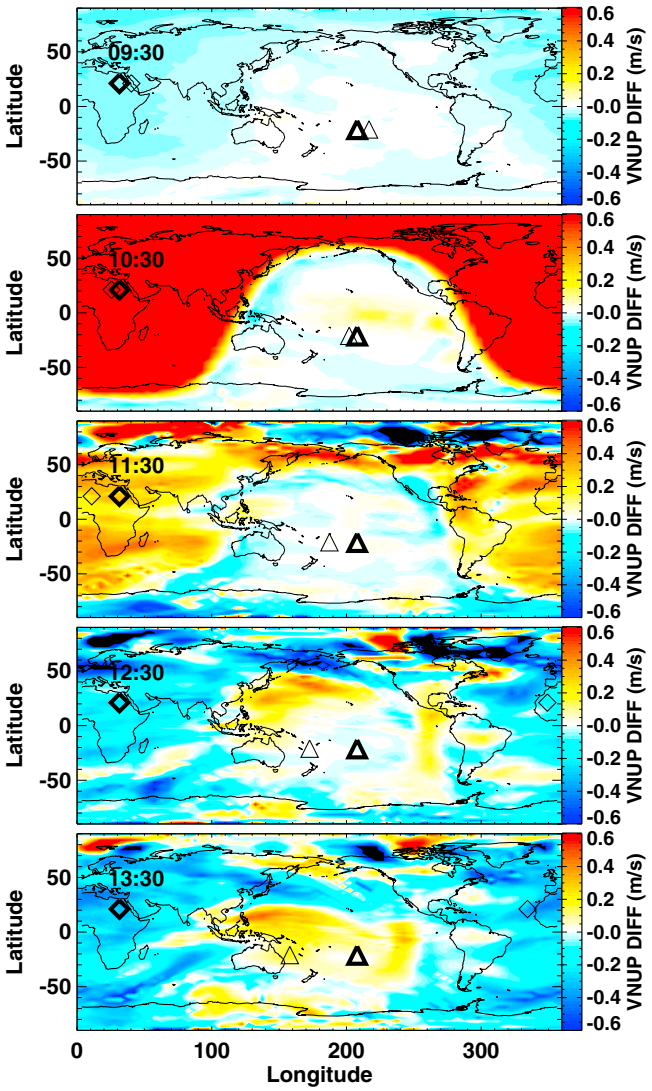

Figure 4. The global map of the differenced low-frequency vertical neutral wind at 0930 UT, 1030 UT, 1130 UT, and 1330 UT. The thick diamond and the thick triangle mark the subsolar and antisubsolar points at the time of the plot; the thin triangles mark the antisubsolar point when the flare occurred (1003 UT).

propagation. The exponential decrease in the neutral mass density causes the amplitudes of the vertical wind to grow in amplitude as $\rho_0^{-1/2}$ accordingly, where ρ_0 is the basic unperturbed neutral density [*Lindzen*, 1967, 1968, 1981; *Hodges*, 1969]. An upward propagating acoustic wave in the thermosphere, caused by a sudden intense enhancement of high-latitude Joule heating, was simulated by *Deng et al.* [2008], who pointed out that the magnitude of the vertical wind perturbation also increased with altitudes.

The small disturbances below 300 km are difficult to observe, as a result of the ever-growing amplitude of vertical propagation waves. To accentuate the amplitude of the low-altitude waves, the attitudinal profiles of the raw vertical wind were scaled according to the square root of the ratio of the neutral mass density at the plotted altitude (ρ) and the background density ($\rho_{400\ \mathrm{km}}$), which gave the normalized vertical wind $VN_{\mathrm{UP.norm}}$ of

$$VN_{\mathrm{UP.norm}} = VN_{\mathrm{UP}} \cdot \sqrt{\frac{\rho}{\rho_{400\ \mathrm{km}}}}. \quad (5)$$

As shown in Figure 6b, the normalized vertical neutral wind shows the perturbation at low altitudes. The perturbation in the vertical wind started from approximately 130 km altitude during the flare. The rapid enhancement in energy deposition at low altitudes led to heating in the lower and middle thermosphere, which drove an enhancement in the vertical pressure gradient.

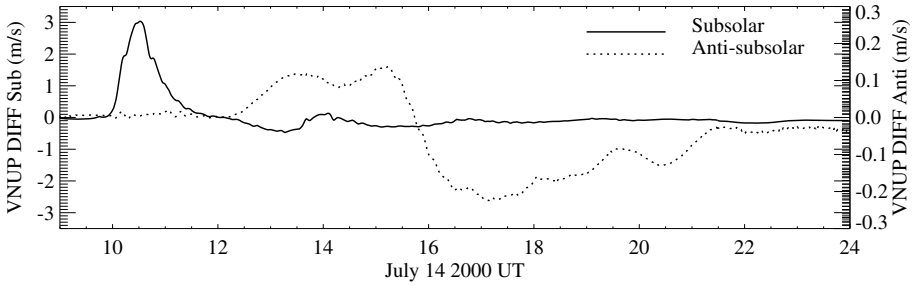

Figure 5. The low-frequency component of the vertical winds at flare-time subsolar (solid line) and antisubsolar (dotted line) points from 0900 UT to 2400 UT on 14 July 2000.

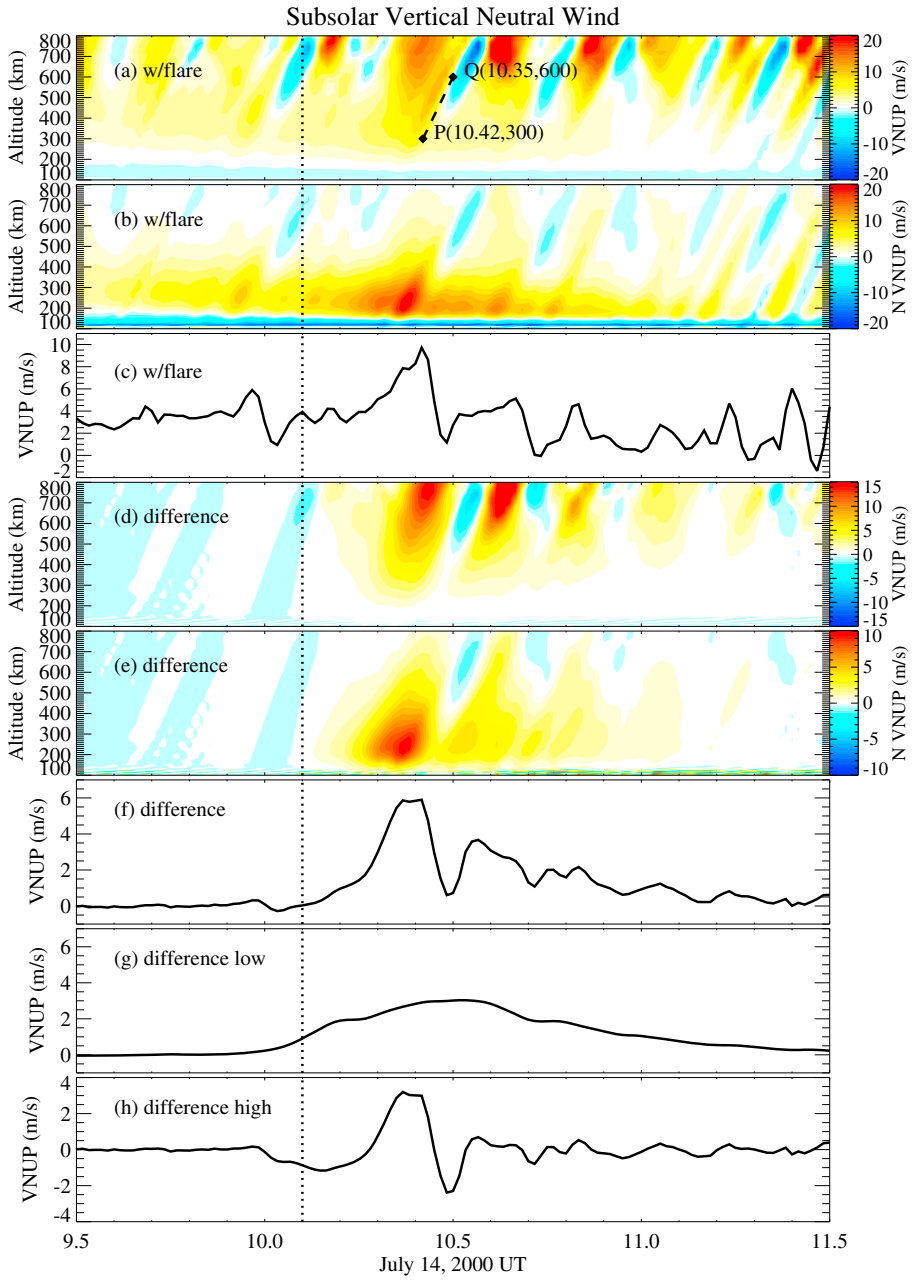

Figure 6. The temporal variation of the vertical neutral wind at subsolar point from 0930 UT to 1130 UT on 14 July 2000. The dashed vertical lines at 1003 UT mark the time of the flare onset. (a) The altitudinal profiles of the raw vertical neutral wind from 100 km to 800 km. (b) The altitudinal profiles of the normalized raw vertical neutral wind. (c) The raw vertical neutral wind at 400 km altitude. (d) The altitudinal profiles of the differenced vertical wind. (e) The altitudinal profiles of the normalized differenced vertical wind. (f) The differenced vertical wind at 400 km altitude. (g) The low-frequency component of the differenced vertical wind at 400 km altitude. (h) The high-frequency component of the differenced vertical wind at 400 km altitude.

This disturbed the hydrostatic equilibrium in the low thermosphere, causing acceleration of the vertical wind accordingly. The source of the acoustic waves will be discussed in more detail below.

Figure 6c shows the raw vertical neutral wind at 400 km altitude. The amplitude of the vertical wind peaked at 10 m/s around 1025 UT. The amplitude of the variation was approximately 7 m/s, with a baseline of 2–3 m/s upward flow. This baseline is simply the dayside lifting of the atmosphere due to the slow thermospheric temperature increase throughout the day time. Figures 6d and 6e show the attitudinal

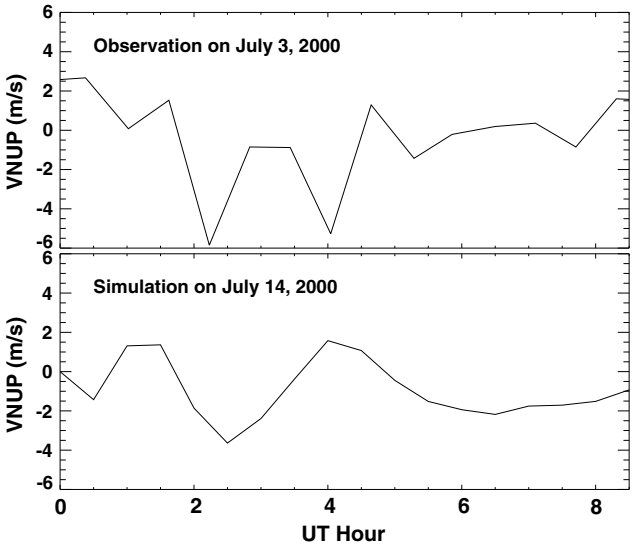

Figure 7. The vertical winds observed by the FPI experiment at (top) Arecibo on 3 July 2000 and that simulated in (bottom) GITM at 300 km altitude at Arecibo on 14 July 2000.

profiles of the differenced vertical wind and the normalized differenced vertical wind, respectively. The amplitude of the flare-driven waves increased with altitudes as expected. Based on the positions, P(10.27, 300) and Q(10.35, 600) in Figure 6a, the vertical propagation speed was calculated as 1042 m/s. It was close to the averaged local sound speed, $\sqrt{\frac{\gamma p}{\rho}}$, of approximately 1074 m/s at 400 km altitude from 0930 UT to 1130 UT in the simulation. Figure 6f shows the differenced vertical wind at 400 km altitude. The flare increased the vertical neutral wind by 6 m/s within 20 min. The perturbations of the acoustic waves due to the flare decreased rapidly and were mostly gone in about 1 h. Note that this perturbation in the differenced vertical wind was a combination of the large-scale gravity wave and the acoustic waves. Figure 6g shows the low-frequency component of the differenced vertical wind in Figure 6f and that the positive phase of the large-scale gravity wave went through the subsolar point (the same as the solid line from 0930 UT to 1130 UT in Figure 5). Figure 6h shows the high-frequency component of the differenced vertical wind (i.e., the acoustic waves). The acoustic wave activity decreased quite quickly after the flare occurred. Both the acoustic waves and the gravity wave had amplitudes of ~3 m/s.

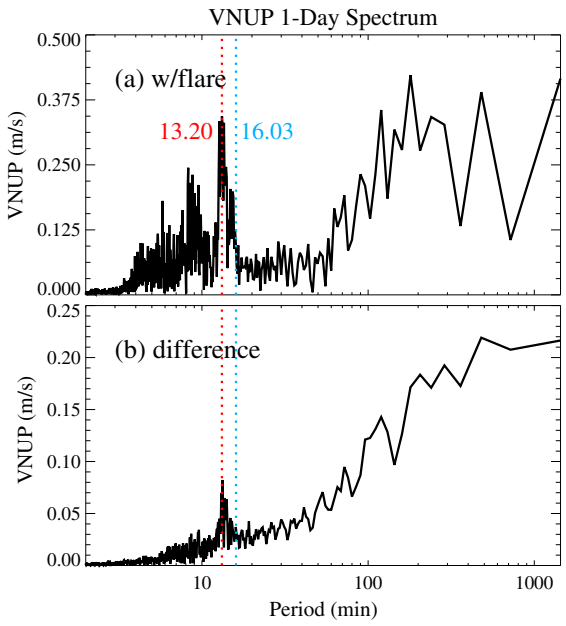

Figure 8. The fast Fourier transforms (FFTs) of the vertical neutral wind at 400 km altitude for 1 day period on 14 July 2000. The blue dashed vertical line marks the average buoyancy period of about 16 min; the red dashed line marks the period where the vertical wind power lies. (a) The 1 day spectrum of the raw vertical neutral wind; (b) the differenced vertical neutral wind.

In order to determine whether these variations are similar to the actual neutral wind, the model results were compared qualitatively with measurements. This is quite difficult to do on the dayside, since most Fabry-Perot Interferometers (FPIs) operate on the nightside only. Further, data from the near-equatorial region was quite limited during this time period. Therefore, data from the Arecibo FPI (18.4°N 66.6°W) on 3 July 2000 was compared to the simulation on 4 July 2000 at the same location as shown in Figure 7. Obviously, an exact match is not expected since these are different days. But, qualitatively, the waves observed in the simulation results (preflare) are comparable to the waves observed by the FPI at Arecibo. The FPI uses the brightness measurements at 630 nm, which gives the wind conditions around 240–250 km [*Friedman and Herrero*, 1982; *Jacka*, 1984; *Hernandez*, 1986]. Figure 7 shows a good agreement in the magnitude of the vertical wind (~5 m/s) between the observation and the simulation results.

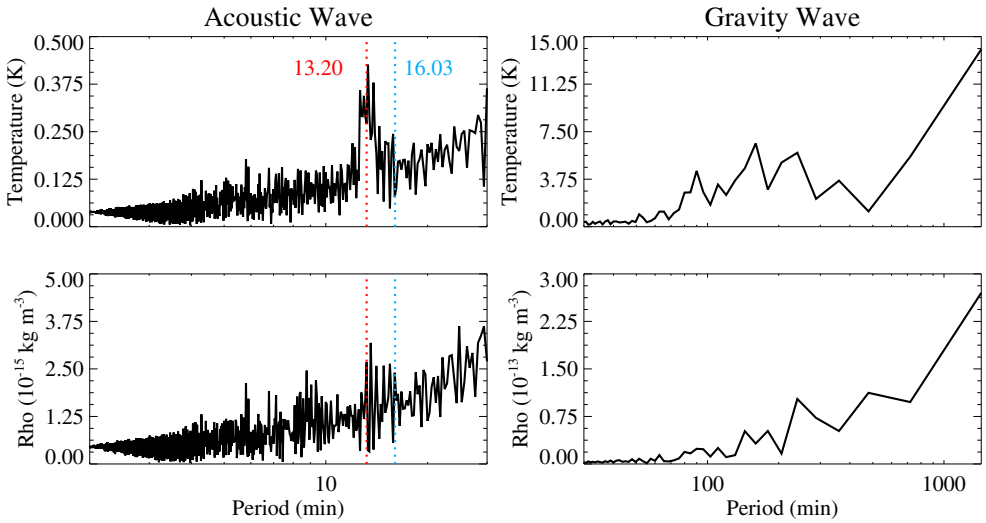

Figure 9. The fast Fourier transforms (FFT) of the neutral (top) temperature and (bottom) density at 400 km altitude for 1 day period on 14 July 2000. (left column) The spectra of the acoustic wave from 0 to 30 min; (right column) the spectra of the gravity waves from 30 min to 24 h. The blue dashed vertical lines mark the average buoyancy period; the red dashed line marks the period where the vertical wind power lies.

4.3. Wave Analysis

Figure 8 shows the Fast Fourier Transform (FFT) of the vertical neutral wind at 400 km altitude for the 1 day period on 14 July 2000. The blue dashed line marks the average buoyancy period of approximately 16 min; the red dashed vertical line marks the period of 13 min where the peak power occurred. Figure 8a shows the FFT of the raw vertical neutral wind, while Figure 8b shows the FFT of the differenced vertical wind.

As previously discussed, the waves with frequencies (periods) that are greater (smaller) than the buoyancy frequency are the acoustic waves, which lie on the left side of the buoyancy period (blue line), while the gravity waves, with frequencies (periods) below (above) the buoyancy frequency, lie on the right side of the buoyancy period. Three peaks existed in the range of the acoustic wave frequencies, of which the period with the most wave energy was 13.2 min. This was also the period in which the differenced vertical wind contained the most energy in the acoustic wave range. As this peak frequency (0.0013 s^{-1}) was comparable to the buoyancy frequency (0.0010 s^{-1}), the potential energy associated with the buoyancy force may have had a similar order of magnitude between the kinetic energy and elastic energy of the acoustics [*Yeh and Liu*, 1974]. Therefore, the acoustic waves that contained the most energy may be highly affected by the buoyancy force. The power above the buoyancy period stayed at a relatively low value until a period of about 60 min, at which point the power increased to a value comparable to the peak in the acoustic wave range. This lack of wave activity possibly indicates the existence of the cutoff region in the acoustic-gravity waves.

One interesting feature to note is that the magnitudes of the acoustic waves around the period of 13 min and the magnitudes of the gravity waves with periods of ~200 min were comparable as shown in the spectra of the vertical wind in Figure 8. However, the amplitudes of the temperature and density perturbations in the gravity waves were approximately 1–2 orders greater than in the acoustic waves. Figure 9 shows the FFT of the raw neutral temperature (top row) and neutral density (bottom row) at 400 km altitude for 24 h on 14 July 2014. Assuming that the waves with periods smaller than the buoyancy period (blue line) were acoustic waves while the waves above the buoyancy period were gravity waves, the left figures (2 min to 30 min) show the spectra of the acoustic waves, while the right figures (30 min to 24 h) show the spectra of gravity waves. In the acoustic wave spectra, there existed a clear power peak at 13.3 min with temperatures similar to the vertical wind (Figure 8). The peak in density was difficult to decipher. The amplitude of the acoustic wave in the temperature was about 0.5 K, while the amplitude of the gravity wave was about 10 K. For the density, the amplitude of the gravity wave was almost 2 orders larger than the magnitude of the acoustic waves. The theoretical ratio of the perturbed density between the gravity

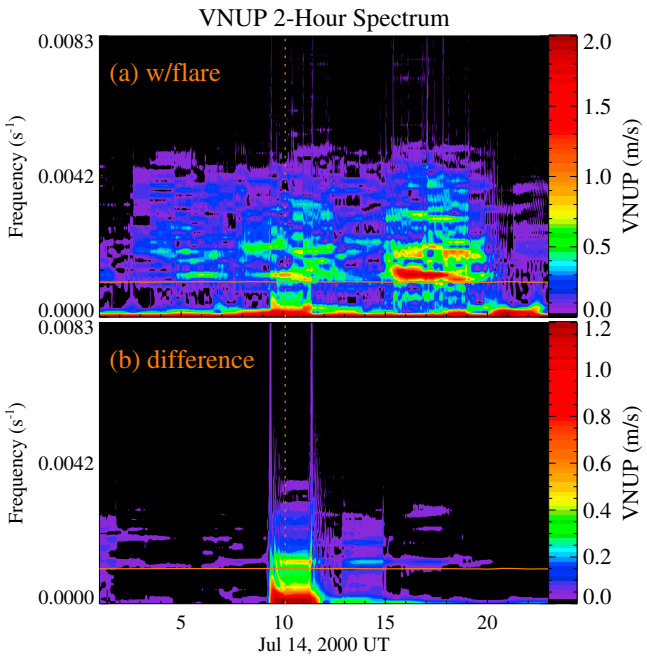

Figure 10. Spectrum of the vertical neutral wind at 400 km altitude within every 2 h window. (top) The spectrum of the flare vertical neutral wind; (bottom) the spectrum of the differenced vertical neutral wind. The red solid line indicates the buoyancy frequency at the centered time of each window. The red dashed line marks the time of the flare onset.

and acoustic waves is $\frac{a_s N^2}{\omega_g g}$ while that of the perturbed pressure between the gravity and acoustic waves is approximately $\frac{N^2}{\omega_g^2}$, where ω_g is the angular frequency of the gravity waves. Assuming the buoyancy frequency N was 10^{-2} rad/s and the angular frequency of the gravity waves was 10^{-3} rad/s, the ratio of the perturbed density and pressure between the gravity wave and acoustic waves were 10 and 100, respectively. Based on a simple ideal gas assumption, the ratio of the perturbed temperature between the gravity and acoustic waves should be 10–100. Note that the ideal gas assumption is not correct for gravity waves, which might introduce some error in the ratio of temperature. These theoretic ratios are in relatively good agreement with the ratios produced by the model.

Figure 10 shows how the power spectrum of the raw vertical wind at 400 km altitude at the subsolar point changes as a function of time using a 2 h window that extended 1 h before and 1 h after the centered time. Figure 10 (top) shows the spectra of the raw vertical wind, while the Figure 10 (bottom) shows the spectra of the differenced vertical wind. The frequency range above the buoyancy frequency (red solid line) contains the spectrum of acoustic waves, and the range below shows that of gravity waves. Before the flare occurred, a small amount of acoustic and gravity wave activity occurred. Most of the acoustic wave energy occurred at a frequency of 0.002 s^{-1} (i.e., a period of 8 min). It can be inferred that gravity waves propagated with varying directions as a function of time before the flare onset, since the range of the forbidden zone appeared to change with time.

There was essentially no wave activity in the differenced vertical neutral wind, because there were essentially no differences in the drivers before the onset of the flare. The flare occurred at 1003 UT as marked by the red dashed vertical line. The perturbation started 1 h ahead in the 2 h spectrum because each window was chosen 1 h before and after the centered time. Extensive acoustic waves were excited by the flare, with a power peak slightly above the buoyancy frequency. Acoustic waves with high frequencies that were above 0.004 s^{-1} (i.e., periods less than 4 min) existed during the flare. The power of the acoustic waves peaked right above the buoyancy frequency. The cutoff zone almost disappeared when the flare occurred. This indicates that the gravity waves that were excited by the flare propagated more horizontally. The cutoff region showed up again around 1200 UT, indicating the time when the horizontally propagating gravity waves died down.

Figure 10 (bottom) shows the 2 h spectra of the differenced vertical wind at the corresponding point. As discussed above, the flare excited extensive acoustic wave and gravity wave activity. Similar to the raw spectra, the power of the acoustic waves in the differenced wind peaked right above the buoyancy frequency. Horizontally propagating gravity waves were also excited at the flare onset and died down in about 2 h. The wave activity due to the second much smaller flare, from 1400 UT to 1500 UT, can be observed in Figure 10 (bottom).

Significant wave activity existed in the raw vertical wind from 1500 UT to 2000 UT. These were caused by the IMF disturbances during this time period. The IMF disturbances drove more intense acoustic waves than

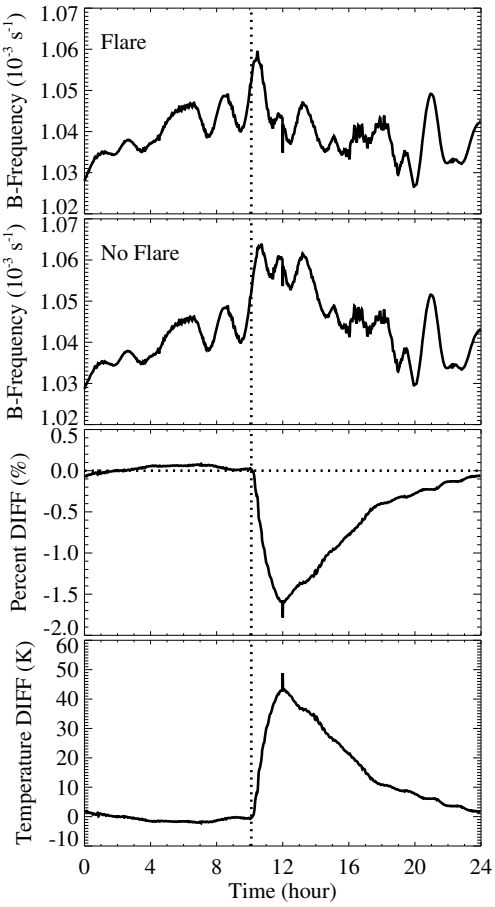

Figure 11. Temporal variation of the subsolar buoyancy frequency at 400 km for the (first row) flare simulation and for the (second row) nonflare simulation for 14 July 2000. (third and fourth rows) The percent difference in buoyancy frequency and the temperature difference due to the flare. The dashed vertical lines mark the flare onset.

gravity waves when compared to those driven by the flare. This means that the flare caused both acoustic waves and a broad spectrum of gravity waves while the IMF disturbances were more likely to excite strong acoustic waves and weak gravity waves of a specific frequency at the subsolar point near the equator.

Figure 11 shows the temporal variations of the buoyancy frequency at the subsolar point at 400 km altitude for the flare simulation (first row) and for the nonflare simulation (second row), respectively, for 14 July 2000. The percent difference in the buoyancy frequency and the temperature difference between the flare and nonflare simulations are shown in the third and fourth rows of Figure 11, respectively. The flare and nonflare simulations show similar variations prior to the flare onset. The buoyancy frequency decreased by almost 2% 2 h after the flare occurred, before it gradually recovered to an undisturbed status. This was because the increase in the solar irradiance enhanced the thermospheric temperature on the dayside when the flare occurred. Under the ideal gas assumption, the sound speed (equation (3)) can be further expressed as follows:

$$a_s = \sqrt{\frac{\gamma nkT}{n\tilde{m}}} = \sqrt{\frac{\gamma kT}{\tilde{m}}}, \tag{6}$$

where k is the Boltzmann constant, n is the number density of the neutrals, T is the neutral temperature, and $\tilde{m}$ is the number density weighed molecular mass. Inserting a_s into equation (2), the buoyancy frequency can be written as follows:

$$N = \sqrt{\frac{\gamma - 1}{\gamma}\frac{\tilde{m}g^2}{kT}}. \tag{7}$$

Since the buoyancy frequency is inversely proportional to the temperature, it decreased when the temperature increased during the solar flare. The influence of the solar flare on the subsolar buoyancy frequency lasted for about 14 h, which is the same time scale of the temperature perturbation.

4.4. Sources of the Wave Generation

Figure 12 shows the temporal variations of the vertical neutral wind (Figures 12a and 12c) and neutral parcel acceleration in the vertical direction (Figures 12b and 12d) between 125 km and 200 km from 0930 UT to 1130 UT. The region below ~125 km was not discussed because there were high-frequency waves existing due to a lack of hydrostatic equilibrium in the lower boundary from Mass Spectrometer Incoherent Scatter. Figures 12a and 12b show the high-frequency variation, while Figures 12c and 12d show the low-frequency variation. The high-frequency results were obtained by subtracting the mean value within a running 30 min window from the original data to remove the lower frequency variability in the acceleration results. The low-frequency components were obtained by subtracting a running 4 h average from the running 30 min average. Thirty minutes and 4 h were chosen because the periods of acoustic

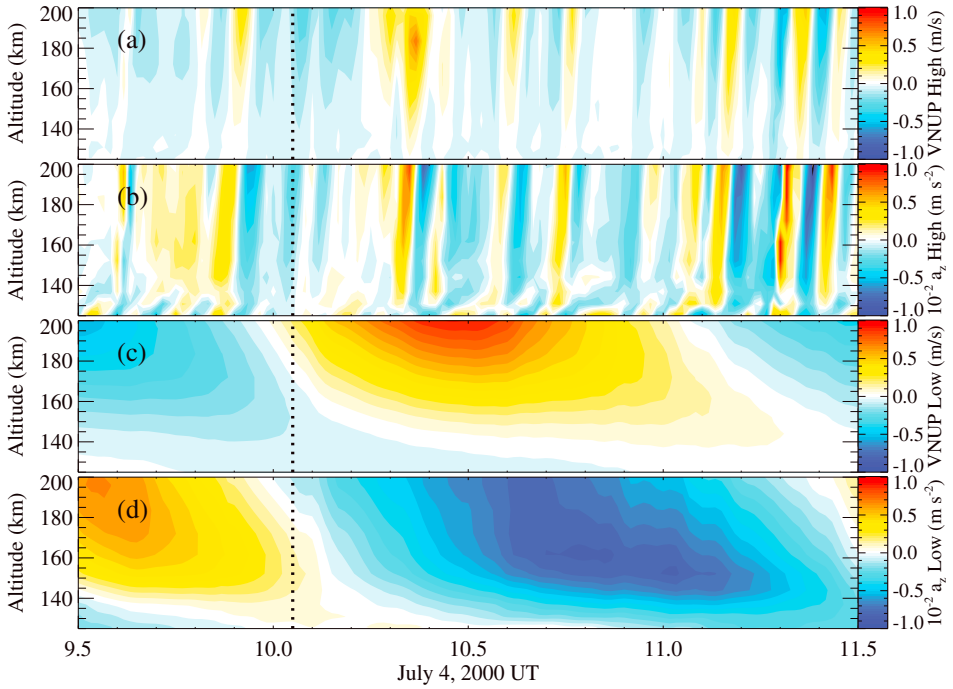

Figure 12. Temporal variation of vertical neutral wind zoomed between 125 km and 200 km from 0930 UT to 1130 UT. (a and b) The high-frequency components of the vertical neutral wind and the neutral parcel acceleration. (c and d) The low-frequency components of the vertical neutral wind and the neural parcel acceleration. The dotted lines mark the flare onset.

waves (~13 min) were well below 30 min, and the periods of the gravity waves (~ 2 h) were between 30 min and 4 h. Therefore, the acoustic and gravity waves should be observed in the high-frequency and low-frequency results, respectively.

The acceleration in the vertical direction a_z was calculated by using

$$a_z = -\frac{1}{\rho}\frac{\partial p}{\partial z} + g, \tag{8}$$

where ρ is the neutral density, p is pressure, z is altitude, and g is the local gravitational acceleration. The variations in the high- and low-frequency components in the acceleration were caused by the variations in the pressure gradient.

Assuming the acoustic waves propagate upward with a wave vector k and the gradient in pressure was the dominant force in the wave propagation, the equation of wave motion in the vertical direction can be expressed as

$$\rho_0\left(\frac{\partial \tilde{u}}{\partial t} + u_0\frac{\partial \tilde{u}}{\partial z}\right) = -\frac{\partial \tilde{p}}{\partial z}, \tag{9}$$

where the background neutral density and vertical velocity are ρ_0 and u_0, respectively, and the perturbation in the pressure and in the vertical velocity are $\tilde{p}$ and $\tilde{u}$, respectively. Consider a wave propagation in form of

$$\tilde{u} = \tilde{u}_0 e^{i(kz-\omega t)}, \qquad \tilde{p} = \tilde{p}_0 e^{i(kz-\omega t)}, \tag{10}$$

where $\tilde{u}_0$ and $\tilde{p}_0$ are the amplitudes of the vertical velocity and pressure in the acoustic waves. Substituting into equation (9) gives the relationship between $\tilde{u}$ and $\tilde{p}$:

$$\tilde{p} = \rho_0\left(\frac{\omega}{k} - u_0\right)\tilde{u}. \tag{11}$$

Consider the dispersion relation of the acoustic waves:

$$\frac{\omega}{k} = a_s, \tag{12}$$

where a_s is the local sound speed as shown in equation (3). Substituting equation (12) into equation (11), and accounting for the fact that the vertical motion u_0 was much less than the local sound speed c_s, there is theoretically a positive phase relation between the pressure and vertical velocity. However, the simulation showed no apparent cross correlation (correlation coefficient of −0.16) between the vertical wind and pressure gradient at 200 km altitude in the acoustic waves (i.e., high-frequency results). Conversely, if the ion drag is also considered as a dominant driver besides the pressure gradient, the wave equation in the vertical direction becomes

$$\rho_0\left(\frac{\partial \tilde{u}}{\partial t} + u_0\frac{\partial \tilde{u}}{\partial z}\right) = -\frac{\partial \tilde{p}}{\partial z} + \rho_i \nu_{in}(u_i - \tilde{u}), \tag{13}$$

where ρ_i is the ion mass density, ν_{in} is the ion-neutral collision frequency, and u_i is the vertical ion velocity. For simplicity, taking the ion velocity as constant of zero and substituting equation (10), the relationship between $\tilde{u}$ and $\tilde{p}$ is

$$\frac{\tilde{p}}{\tilde{u}} = \frac{\rho_0}{k}\left[(\omega - ku_0) + \mathbf{i}\nu_{\mathrm{in}}\right]. \tag{14}$$

Equation (14) can be rewritten as

$$\frac{\tilde{p}}{\tilde{u}} = \frac{\rho_0}{k}((x + \mathbf{i}y), \tag{15}$$

where $x = \omega - ku_0 \approx \omega$ and $y = \nu_{\mathrm{in}}$. Equation (15) can further be written as

$$\frac{\tilde{p}}{\tilde{u}} = \frac{\rho_0}{k}\sqrt{x^2 + y^2}(\cos\theta + \mathbf{i}\sin\theta) = \frac{\rho_0}{k}\sqrt{x^2 + y^2}e^{\mathbf{i}\theta}, \tag{16}$$

where

$$\theta = \arccos\frac{x}{\sqrt{x^2 + y^2}}. \tag{17}$$

This indicates that there was a phase delay of θ between the waves in the vertical velocity and the pressure. Because $\sin\theta > 0$ and $\cos\theta > 0$, the delayed phase θ was between 0 and $\frac{\pi}{2}$. Taking the ion-neutral collision frequency as 0.06 s^{-1} ($\nu[O^+, O_2]$ at 200 km) [*Schunk and Nagy*, 2009] and the frequency of the acoustic waves as ω =0.02 rad/s, there existed a phase delay of approximately $\frac{7}{18}\pi$. The average buoyancy period at 200 km was approximately 14.5 min. Taking the phase delay of $\frac{7}{18}\pi$, a real time delay of 2.82 min would be expected between the vertical velocity and the pressure. In the simulation, a maximum correlation of 0.52 was reached at a time delay of 2 min. The effect of the ion drag on the vertical neutral motion will be discussed in more detail below.

The vertical wind and the vertical acceleration were anticorrelated in the gravity waves with a correlation coefficient of −0.67 at 200 km altitude as shown in Figures 12c and 12d. The theoretical ratio between the perturbation pressure and the vertical perturbation velocity in the gravity waves in the thermosphere is

$$\frac{\tilde{p}}{\tilde{u}} = -\frac{\rho_0}{\omega k}(N^2 - \omega^2), \tag{18}$$

where ρ_0 is the background neutral density and k is the wave number in the vertical direction such that $k > 0$ when the phase speed is upward [*Kundu and Cohen*, 2008]. Because the frequencies of the gravity waves were smaller than the buoyancy frequency, i.e, $\omega^2 < N^2$, the vertical velocity in the gravity waves was inversely proportional to the perturbation in pressure gradient. This anticorrelation was well modeled in the simulation. Therefore, the nonhydrostatic equilibrium due to the perturbation in the pressure gradient was the main source of the gravity waves. In order to better show the large-scale gravity wave activity, the low-frequency components of the vertical wind and vertical acceleration from 0000 UT to 2400 UT are shown in Figure 13. The phase speed of the gravity waves was downward as expected. The periods of the gravity waves were approximately 2–3 h.

The correlation between the perturbation in the vertical motion and the perturbation in the pressure gradient in both the acoustic waves and the gravity waves show good agreement between the simulation results and the theoretical calculations. This leads to an inference that the gradient in pressure was the driver

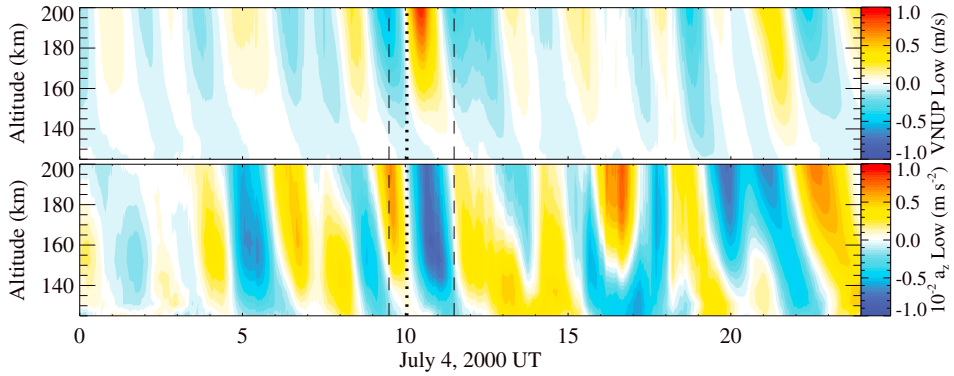

Figure 13. The temporal variation of vertical neutral wind between 100 km and 200 km from 0000 UT to 1130 UT. (top and bottom) The low-frequency vertical wind and the parcel acceleration. The time frame between the two dashed lines is from 0930 UT to 1130 UT. The dotted lines mark the flare onset.

of the two waves and that the ion drag force caused a phase delay between the pressure gradient variations and the vertical motion in the acoustic waves.

Figure 14 shows vertical profiles of the subsolar percentage changes in the neutral temperature, mass density, and pressure, as well as the difference in the vertical acceleration with respect to 10:06 UT. The temporal change of the vertical acceleration was caused primarily by the change in the pressure gradient since gravity does not change with time. The six colored lines represent six UTs between the flare onset and the flare peak. The temperature increased by approximately 0.4% at maximum around 140 km because of the increase in heating due to the flare. The temperature decreased above 200 km altitude. The mass density increased by $\sim$ 0.9% around 250 km and decreased both in the regions below 130 km and above 320 km. The causes of these changes in the high-altitude temperature and the mass density are still unclear to us and need further study. The combination of the changes in temperature and mass density led to a net increase in the pressure around 200 km and a decrease in the pressure above ~300 km. The spatial and temporal variations in the pressure further led to the perturbations in the vertical acceleration of the neutral particles at different altitudes, as is shown in Figure 14 (first column). These perturbations thus started launching the thermospheric gravity and acoustic waves, as described above.

4.5. Acoustic Waves Generated by Penetration Electric Fields

Figure 15 shows the high-frequency components of the neutral and ion vertical winds as well as the dynamo electric field at 400 km at the subsolar and antisubsolar locations. The high-frequency component was obtained by subtracting a running 30 min average from the simulation data. There exists an anticorrelation

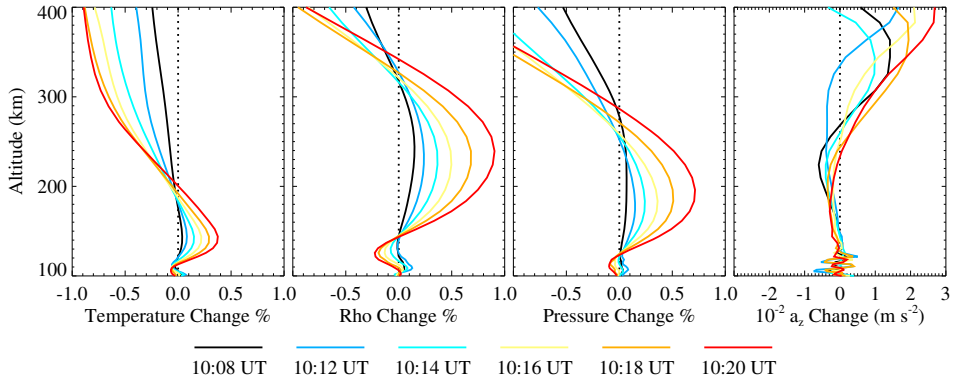

Figure 14. (first to fourth columns) The vertical profiles of the percentage changes in the subsolar neutral temperature, mass density, and pressure, as well as the difference in the vertical acceleration with respect to 10:06 UT. For example, the yellow line in Figure 14 (first column) shows $\frac{T_{1016}-T_{1006}}{T_{1006}} \times 100\%$, while in Figure 14 (fourth column) shows $a_{z1016} - a_{z1006}$. The six colored lines represent six UTs as indicated below. The vertical dashed line marks "zero" change.

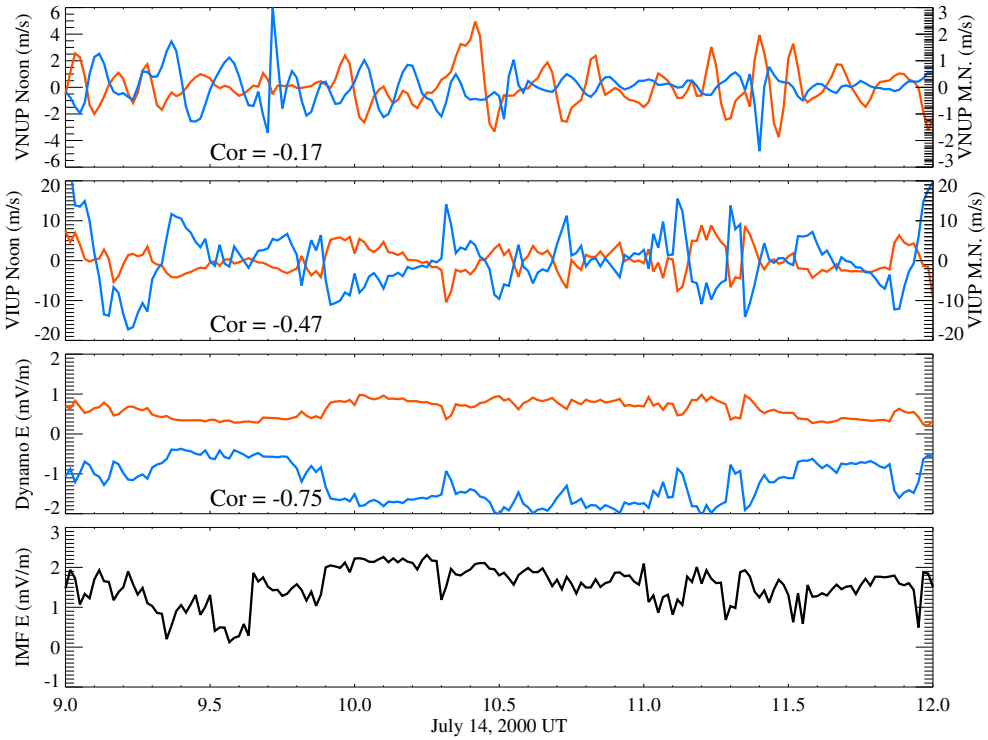

Figure 15. (first row) The temporal variation of the high-frequency component of the raw vertical neutral wind, (second row) the high-frequency component of the raw vertical ion velocity, and (third row) the zonal dynamo electric field. The red and blue lines show the data on the subsolar and antisubsolar sectors, respectively. (fourth row) The temporal variation of the high-latitude electric field driven by the interplanetary magnetic field.

between the dayside and nightside flows. This can be quantified through a cross correlation of −0.17 for the neutrals and −0.47 for the ions.

As shown in Figure 15 (third row), the subsolar (red line) and the antisubsolar (blue line) zonal dynamo electric fields were anticorrelated with a cross correlation of −0.75. A dawn-to-dusk electric field existed in the equatorial ionosphere, resulting in an eastward electric field on the dayside near the magnetic equator, and a westward electric field on the nightside. With the combination of the northward magnetic field, the eastward (westward) electric field on the dayside (nightside) caused upward (downward) drifts of the ions. This is shown in Figure 15 (third row), where the vertical ion velocity is positively correlated with changes in the dynamo electric field. The plotted ion drifts are the high-frequency component, while the electric field is not filtered. This indicates that the rapid variations in the vertical motion of the ions were controlled by the changes in the dynamo electric field. The dynamo electric field is primarily determined by the divergence of currents driven by neutrals colliding into ions, forcing them to move in the neutral wind direction. This divergence creates field-aligned currents that drives the *F* region electric field [*Maeda and Kato*, 1966; *Kelley*, 2009]. Further, the low-latitude electric field is driven by the penetration of the magnetospherically driven high-latitude electric field to lower latitudes [*Nishida*, 1968; *Kelley et al.*, 1979; *Huang and Foster*, 2005]. These penetration electric fields may change rapidly due to the variability in the high-latitude ion flows.

The changes in the electric field observed in the equatorial region were strongly correlated with the interplanetary electric field (Figure 15, fourth row). The IMF-driven electric field E_{IMF} was calculated based on the formula:

$$E_{IMF} = V_s B_s \sin(\theta/2), \tag{19}$$

where V_s is the solar wind speed in the sunward direction, $B_s = (B_y{}^2 + B_z{}^2)^{\frac{1}{2}}$, and θ is the angle between the two components of the IMF, B_y and B_z [*Kan and Lee*, 1979]. The correlation between low-latitude ion drifts and the interplanetary electric field has been confirmed by observations, which showed the variations in the observed dayside ionospheric electric field at middle and low latitudes in association with

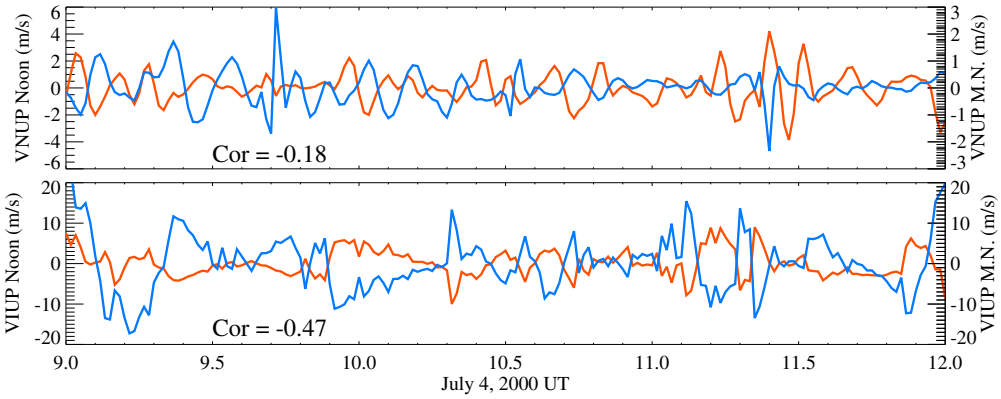

Figure 16. The temporal variation of the (top) high-frequency component of the raw vertical neutral wind without the flare and the (bottom) high-frequency component of the raw vertical ion velocity without the flare. The red and blue lines show the data on the subsolar and antisubsolar sectors, respectively.

the IMF electric field [*Huang and Foster*, 2005]. Practically in GITM, the high-latitude electric fields (driven by the IMF and solar wind) penetrate to the equator via the high-latitude boundary condition on the dynamo solver, which was placed at 65° magnetic latitude, allowing some of the potential to leak to lower latitudes. Since the *Weimer* [2005] empirical electric field model was used in this study, with an update time of 1 min, any variations in the IMF or solar wind velocity caused changes in the high-latitude potential pattern and the boundary of the dynamo solver. This resulted in changes in the low-latitude dynamo potential, and therefore the low-latitude electric field. As shown in Figure 15 (third and fourth rows), the dynamo electric field at the subsolar point generally had a positive correlation with the IMF-driven electric field (0.7), while the electric field at the antisubsolar point was negatively correlated with the interplanetary electric field (−0.7). This was because the projection of the eastward interplanetary electric field in the high latitudes to the equatorial region resulted in an eastward electric field on the dayside and a westward electric field on the nightside.

The high-frequency component of the vertical neutral velocity appeared to be driven by rapid variations in the ion flows which were most likely driven by the rapid variations in the dynamo electric field. The variability of the vertical ion velocity was approximately 3 times greater than that of the vertical neutral velocity. The high-frequency component of the vertical neutral wind was a consequence of the combination of the vertical ion drag pushing the neutrals up and down, and a restoring force to bring the atmosphere back to a hydrostatic equilibrium. Both gravity and the gradient in pressure can act as a restoring force at the wave frequencies (periods of ∼15 min) near the buoyancy frequency [*Yeh and Liu*, 1974].

In order to thoroughly explore the cause of the anticorrelation between the dayside and nightside wave activity, three additional simulations were conducted. First, the high-frequency components in the vertical neutral and ion velocities in the nonflare simulation were explored as shown in Figure 16. Without the perturbation due to the flare, the cross correlations were −0.18 for the neutrals and −0.47 for the ions, which were similar to those with the flare. This indicates that the fluctuations in solar irradiance due the flare did not lead to the anticorrelations.

Second, a simulation with the solar flare turned on, but the dynamo turned off, was conducted to further investigate the role of the dynamo electric field in producing the anticorrelation. As shown in Figures 17, the day-night correlations in the high-frequency components of the vertical neutral wind were −0.17 with dynamo on (top), 0.01 with dynamo off (middle), and −0.21 in the difference between the dynamo on and the dynamo off simulations (bottom). By removing the perturbation due to the flare (bottom), the anticorrelation due to the dynamo electric field was enhanced to −0.21. This indicates that the dynamo electric field, instead of the flare, was the primary factor causing the anticorrelation in the neutrals. Figure 18 shows the day-night correlation in the high-frequency component of the vertical ion velocity in the same format as Figure 17. The correlation coefficient was positive (0.45) in the dynamo off case (middle) and was reduced to −0.60 when only the perturbation caused by dynamo existed (bottom). Therefore, the dynamo electric field also was primarily responsible for the anticorrelation in the ions.

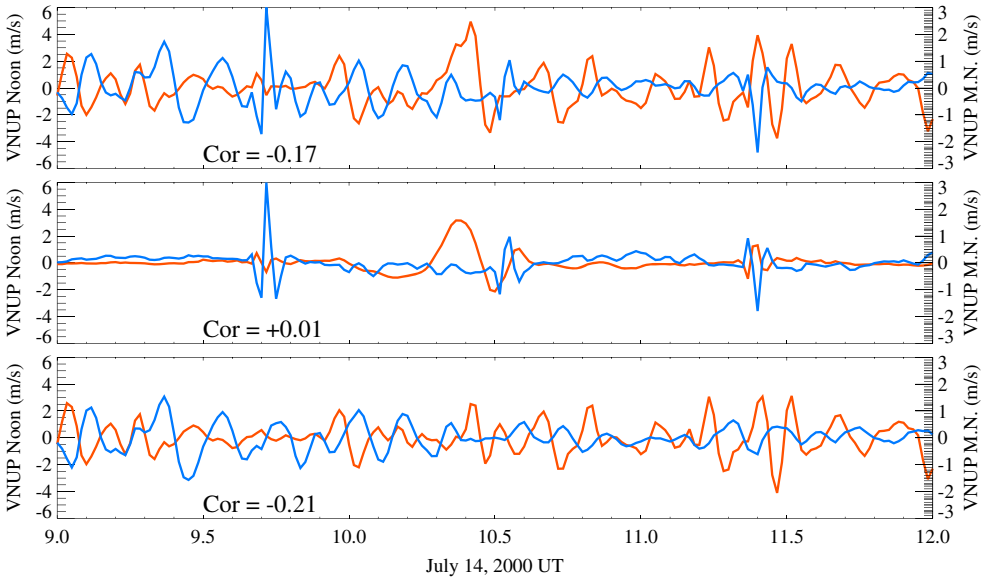

Figure 17. The temporal variation of the (top) high-frequency component of the raw vertical neutral wind with dynamo on, the (middle) high-frequency component of the raw vertical neutral wind with dynamo off, and the (bottom) difference in high-frequency component of the raw vertical neutral wind between dynamo on and dynamo off. The red and blue lines show the data on the subsolar and antisubsolar sectors, respectively.

Finally, a simulation that included the flare had the dynamo on and a constant solar wind input of $B_x = 0.0$, $B_y = 0.0$, $Bz = -2.0$, and $Vx = 400.0$ km/s and was conducted to exclude the possibility that the solar irradiance-induced dynamo field caused the anticorrelation. As shown in Figure 19, the day-night correlations in the high-frequency components of the vertical neutral velocity were −0.17 (top) with the measured IMF input, 0.05 with the constant IMF input (middle), and −0.18 in the difference between the simulations using the measured IMF and the constant IMF inputs (bottom). This means that the variation in the IMF, instead of the variation in the solar irradiance, drove the anticorrelation in the neutrals. Figure 20 shows the day-night correlation in the high-frequency components of the vertical ion velocity in the same

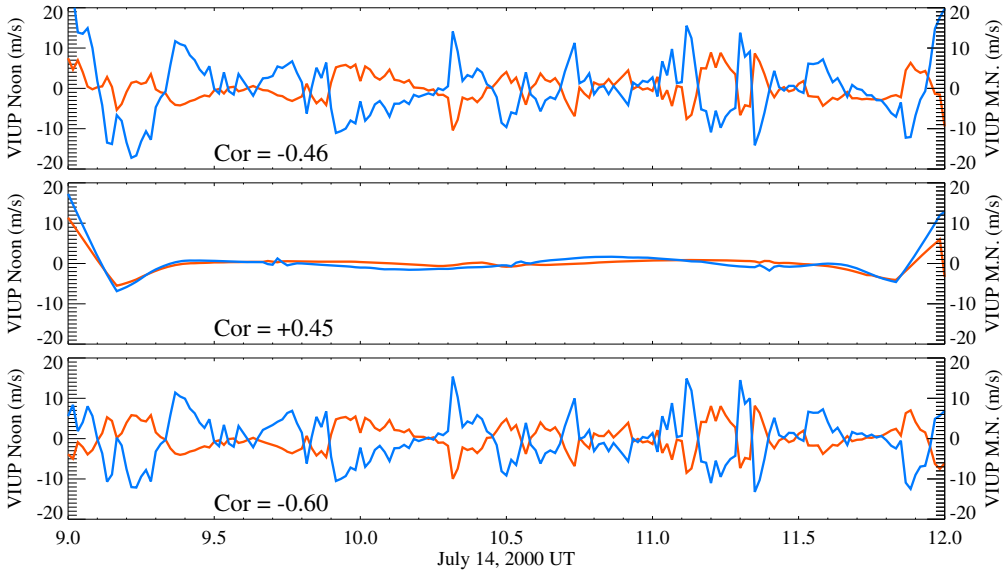

Figure 18. The temporal variation of the (top) high-frequency component of the raw vertical ion velocity with dynamo on, the (middle) high-frequency component of the raw vertical ion velocity with dynamo off, and the (bottom) difference in high-frequency component of the raw vertical ion velocity between dynamo on and dynamo off. The red and blue lines show the data on the subsolar and antisubsolar sectors, respectively.

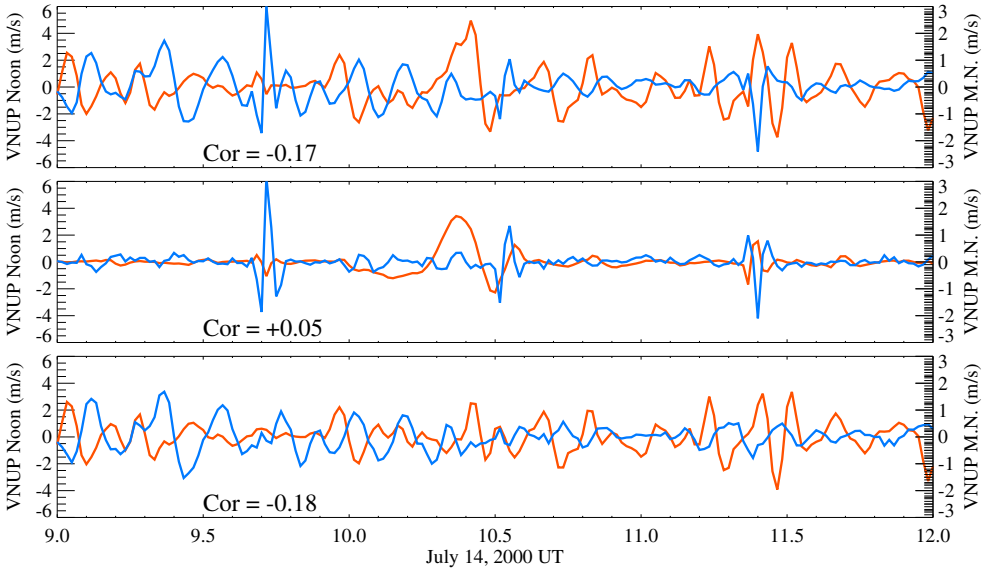

Figure 19. The temporal variation of the (top) high-frequency component of the raw vertical neutral wind with the satellite IMF input, the (middle) high-frequency component of the raw vertical neutral wind with the constant IMF input, and the (bottom) difference in high-frequency component of the raw vertical neutral wind between the satellite IMF and constant IMF. The red and blue lines show the data on the subsolar and antisubsolar sectors, respectively.

format as Figure 19. The correlation coefficient was 0.35 with the constant IMF input but with the flare (middle) and was decreased to −0.60 when only the dynamo field due to the IMF existed (bottom). This means that the variations in the penetration electric field, rather than the dynamo field induced by the solar irradiance, resulted in the anticorrelation in the ions. In summary, the penetration electric field was primarily responsible for the anticorrelation in the high-frequency components of the vertical motion between the dayside and nightside atmosphere.

The relatively low correlation between the vertical ion drifts on the dayside and nightside (i.e., −0.47) is most likely due to the dramatic difference in the dayside and nightside conductivity and the structure of

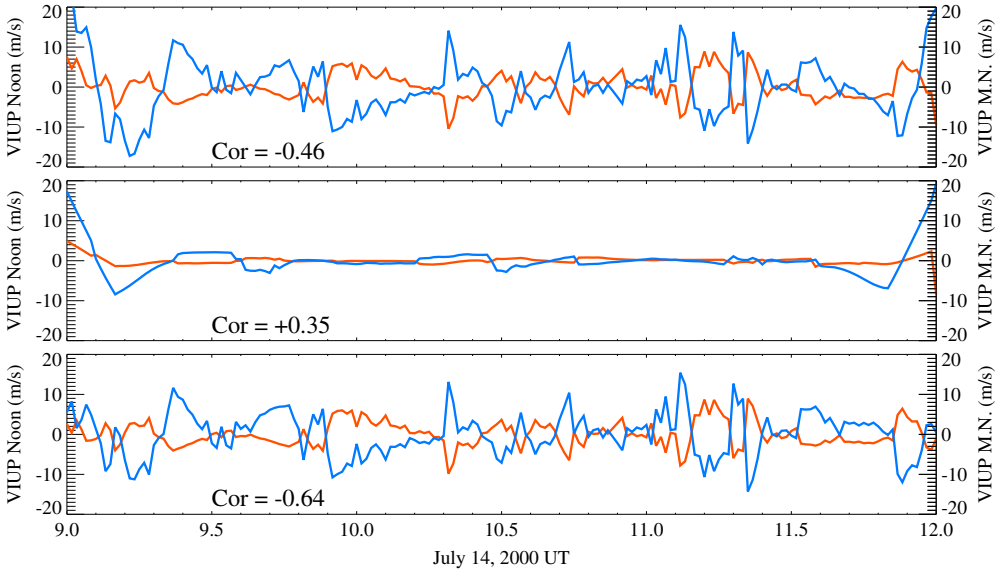

Figure 20. The temporal variation of the (top) high-frequency component of the raw vertical ion velocity with the satellite IMF input, the (middle) high-frequency component of the raw vertical ion velocity with the constant IMF input, and the (bottom) difference in high-frequency component of the raw vertical ion velocity between the satellite IMF and constant IMF. The red and blue lines show the data on the subsolar and antisubsolar sectors, respectively.

the high-latitude electric field in the noon and midnight sectors. Further, the magnetic field structure has significant longitudinal variation, so even if the electric field were exactly anticorrelated between the dayside and nightside, the velocity due to E × B drifts would be different. It is argued here that the ion drifts drive neutral vertical motion, which causes high-frequency waves to occur. This means that because the ion motion only has a correlation of −0.47, the neutral motion must have a worse correlation than this. Given that the ion drag force is dependent on the electric density and the neutral mass density, which are very different on the dayside and nightside of the Earth, it is no surprise that the correlation between the dayside and nightside vertical winds is only −0.17.

It should be mentioned that the treatment of the penetration electric field in the model is not sufficiently physical, because the simulations used the IMF as the only source of the high-latitude electric field, and the *Weimer* [2005] model does not allow the electric field to penetrate to low latitudes by default. GITM gets around this by putting an artificial boundary at a fixed location, allowing the potential to penetrate to the equator. This method does not accurately represent the electrodynamics that actually occurs in the magnetosphere-ionosphere system but allows the physical processes to be approximated. However, the model suggests a mechanism that the neutral waves at low latitudes can be driven by the high-latitude electric field through coupling with ions when penetration electric fields are present.

5. Summary and Conclusion

The nonhydrostatic waves surrounding the 14 July 2000 solar flare were investigated by using the Global Ionosphere Thermosphere Model. The results show that the sudden enhancements in EUV and X-ray fluxes during a solar flare can cause rapid enhancements in the thermospheric temperature at low altitudes, which can drive acoustic and gravity waves. Gravity waves with frequencies well below the buoyancy frequency appear to travel from the dayside to the nightside [*Pawlowski and Ridley*, 2008] and converge at the longitudinal sector which was the antisubsolar point when the flare occurred instead of the antisubsolar point at the time of arrival (about 3.5 h later). Acoustic waves appear to propagate vertically from the low-altitude source region with ever-increasing amplitudes. The wave spectra of the vertical neutral wind show that the acoustic waves have a power peak at approximately 13 min during the flare. The flare caused horizontally propagating gravity waves that decreased the cutoff region, where no propagational waves exist. The flare also caused a decrease in the buoyancy frequency in the subsolar thermosphere of approximately 2%, but this change may not easily be observed in measurements since it is mostly likely smaller than measurement errors. The amplitudes of the acoustic waves and gravity waves were similar in the vertical neutral wind, while the amplitudes of the gravity waves were about 1–2 orders of magnitude greater than the acoustic waves in the neutral density and temperature, as expected. The gradient in pressure was the driver of both the gravity and acoustic waves, while the ion drag caused a phase delay of approximately $\frac{7}{18}\pi$ at 200 km between the variations in the pressure gradient and the vertical velocity in the acoustic waves.

There existed an anticorrelation in the high-frequency component of the vertical neutral wind between the subsolar and antisubsolar points a couple of hours after the flare occurred. This anticorrelation appears to have been driven by the rapid variations of the ion flows due to the dynamo electric field. Variations in the dynamo electric field were controlled by the penetration of high-latitude electric field, driven by the interplanetary magnetic field, to low latitudes. The penetration of IMF-driven electric field to the equatorial regions resulted in an eastward and a westward electric field on the dayside and nightside, respectively. Neutrals were perturbed by ion drag then restored to a near-hydrostatic condition, resulting in waves with frequencies that were close to the characteristic neutral buoyancy frequency. During the flare, the anticorrelation in the high-frequency neutral wind between the subsolar and antisubsolar points was disturbed due to the excitation of acoustic waves on the dayside by the flare.

Acknowledgments

This work was partially supported by NASA grant NNX09AJ59G. We are also deeply indebted to P. Chamberlin for the FISM output that drove GITM for the flare event. The link to the FISM data center is http://lasp.colorado.edu/lisird/fism/. Further, GITM utilized the ACE magnetometer and SWEPAM measurements as well. The link to the ACE data depository is http://www.srl.caltech.edu/ACE/ASC/level2/index.html, and the data are also available at http://cdaweb.gsfc.nasa.gov/. The National Oceanic and Atmospheric Administration (NOAA) provided hemispheric power index data (http://www.swpc.noaa.gov/ftpmenu/lists/hpi.html) to drive the high-latitude auroral precipitation for this event. The wind data observed by FPI at Arecibo is available at http://cedar.openmadrigal.org/. The GITM simulation data for this case are available upon request from the authors.

Alan Rodger thanks the reviewers for their assistance in evaluating this paper.

References

Brunt, D. (1927), The period of simple vertical oscillations in the atmosphere, *Q. J. R. Meteorol. Soc.*, *53*, 30–31, doi:10.1002/qj.49705322103.

Chamberlin, P. C., T. N. Woods, and F. G. Eparvier (2007), Flare irradiance spectral model (FISM): Daily component algorithms and results, *Space Weather*, *5*, S07005, doi:10.1029/2007SW000316.

Coster, A., and A. Komjathy (2008), Space weather and the Global Positioning System, *Space Weather*, *6*, So6D04, doi:10.1029/2008SW000400.

Davides, K. (1990), *Ionospheric Radio*, Peter Peregrinus Ltd., London.

Deng, Y., A. D. Richmond, A. J. Ridley, and H. Liu (2008), Assessment of the non-hydrostatic effect on the upper atmosphere using a general circulation model (GCM), *Geophys. Res. Lett.*, *35*, L01104, doi:10.1029/2007GL032182.
Donnelly, R. F. (1967), The solar flare radiation responsible for sudden frequency deviations, *J. Geophys. Res.*, *101*, 5247–5256, doi:10.1029/95JA03676.
Fejer, B. G., C. A. Gonzales, D. T. Farley, M. C. Kelley, and R. F. Woodman (1979), Equatorial electric fields during magnetically disturbed conditions: 1. The effect of the interplanetary magnetic field, *J. Geophys. Res.*, *84*, 5797–5802, doi:10.1029/JA084iA10p05797.
Friedman, J. F., and F. A. Herrero (1982), Fabry-Perot interferometer measurements of thermospheric neutral wind gradients and reversals at Arecibo, *Geophys. Res. Lett.*, *9*, 785–788, doi:10.1029/GL009i007p00785.
Garriott, O. K., A. V. da Rosa, M. J. Davis, and J. O. G. Villard (1967), Solar flare effects in the ionosphere, *J. Geophys. Res.*, *72*, 6099–6103, doi:10.1029/JZ072i023p06099.
Gombosi, T. I. (1998), *Physics of the Space Environment*, Cambridge Univ. Press, New York.
Gossard, E. E., and W. H. Hooke (1975), *Waves in the Atmosphere*, Elsevier Scientific Company, Amsterdam.
Hernandez, G. (1986), *Fabry-Perot Interferometers*, Cambridge Univ. Press, Cambridge, England.
Hodges, R. R. (1969), Eddy diffusion coefficients due to instabilities in internal gravity waves, *J. Geophys. Res.*, *74*, 4087–4090.
Huang, C. S., and J. C. Foster (2005), Long-duration penetration of the interplanetary electric field to the low-latitude ionosphere during the main phase of magnetic storms, *J. Geophys. Res.*, *110*, A11309, doi:10.1029/2005JA011202.
Huffman, R. E. (1969), Absorption cross-sections of atmospheric gases for use in aeronomy, *Can. J. Chem.*, *47*, 1823–1834, doi:10.1139/v69-298.
Jacka, F. (1984), Application of Fabry-Perot spectrometers for measurement of upper atmosphere temperatures and winds, *Handbook for MAP*, *13*, 19–40, doi:10.1007/BF00179215.
Jones, T. B. (1971), VLF phase anomalies due to a solar X-Ray flare, *J. Atmos. Sol. Terr. Phys.*, *33*, 963–965.
Kan, J. R., and L. C. Lee (1979), Energy coupling function and solar wind-magnetosphere dynamo, *Geophys. Res. Lett.*, *6*, 577–580, doi:10.1029/GL006i007p00577.
Kato, S. (1956), Horizontal wind systems in the ionospheric E-region deduced from the dynamo theory of the geomagnetic S_q variation 2. Rotating Earth, *J. Geomagn. Geoelec.*, *8*, 24–37.
Kato, S. (1957), Horizontal wind systems in the ionospheric E-region deduced from the dynamo theory of the geomagnetic S_q variation 4, *J. Geomagn. Geoelec.*, *9*, 107–115.
Kelley, M. C. (2009), *The Earth's Ionosphere: Plasma Physics and Electrodynamics*, Elsevier Inc., Burlington, Mass.
Kelley, M. C., B. G. Fejer, and C. A. Gonzales (1979), An explanation for anomalous equatorial ionospheric electric field associated with a northward turning of the interplanetary field, *Geophys. Res. Lett.*, *6*, 301–304, doi:10.1029/GL006i004p00301.
Kikuchi, T., H. Luhr, K. Schlegel, H. Tachihara, M. SHinohara, and T. I. Kitamura (2000), Penetration of auroral electric fields to the equator during a substorm, *J. Geophys. Res.*, *105*, 23,251–23,261, doi:10.1029/2000JA900016.
Kundu, P. K., and I. M. Cohen (2008), *Fluid Mechanics*, 4th ed., Academic Press, Elsevier, Burlington, Mass.
Lindzen, R. S. (1967), Thermally driven diurnal tide in the atmosphere, *Q. J. R. Meteorol. Soc.*, *93*, 18–42, doi:10.1002/qj.49709339503.
Lindzen, R. S. (1968), The application of classical atmospheric tidal theory, *Proc. R. Soc. London, Ser. A.*, *303*, 229–316.
Lindzen, R. S. (1981), Turbulence and stress owing to gravity wave and tidal breakdown, *J. Geophys. Res.*, *86*, 9707–9714, doi:10.1029/JC086iC10p09707.
Liu, H., H. Lühr, S. Watanabe, W. Köhler, and C. Manoj (2007), Contrasting behavior of the thermosphere and ionosphere in response to the 28 October 2003 solar flare, *J. Geophys. Res.*, *112*, A07305, doi:10.1029/2007JA012313.
Maeda, K., and S. Kato (1966), Electrodynamics of the Ionosphere, *Space Sci. Rev.*, *5*, 57–79, doi:10.1007/BF00179215.
Maruyama, N., A. D. Richmond, T. J. Fuller-Rowell, M. V. Codrescu, S. Sazykin, F. R. Toffoletto, R. W. Spiro, and G. H. Millward (2008), Interaction between direct penetration and disturbance dynamo electric fields in the storm-time equatorial ionosphere, *Geophys. Res. Lett.*, *35*, L18105, doi:10.1029/2008GL035155.
Mendillo, M., et al. (1974), Behavior of the ionospheric F region during the great solar flare of August 7, 1972, *J. Geophys. Res.*, *79*, 665–672, doi:10.1029/JA079i004p00665.
Nishida, A. (1968), Coherence of geomagnetic dp 2 fluctuations with interplanetary magnetic variations, *J. Geophys. Res.*, *73*, 5549–5559, doi:10.1029/JA073i017p05549.
Pawlowski, D. J., and A. J. Ridley (2008), Modeling the thermospheric response to solar flares, *J. Geophys. Res.*, *113*, A10309, doi:10.1029/2008JA013182.
Richmond, A. D. (1989), Modeling the ionosphere wind dynamo: A review, *Pure Appl. Geophys.*, *131*, 413–435, doi:10.1007/978-3-0348-9280-3_7.
Richmond, A. D. (1995), Ionospheric electrodynamics using magnetic apex coordinates, *J. Geomagn. Geoelec.*, *47*, 91–212.
Rideout, W., and A. Coster (2006), Automated GPS processing for global total electron content data, *GPS Solutions*, *10*, 219–228, doi:10.1007/s10291-006-0029-5.
Ridley, A., Y. Deng, and G. Tòth (2006), The global ionosphere-thermosphere model, *J. Atmos. Sol. Terr. Phys.*, *68*, 839–864, doi:10.1016/j.jastp.2006.01.008.
Ridley, A. J. (2000), Estimations of the uncertainty in timing the relationship between magnetospheric and solar wind processes, *J. Atmos. Sol. Terr. Phys.*, *62*, 757–771, doi:10.1016/S1364-6826(00)00057-2.
Sastri, J. H., J. V. S. V. Rao, D. R. K. Rao, and B. M. Pathan (2001), Daytime equatorial geomagnetic H field response to the growth phase and expansion phase onset of isolated substorms: Case studies and their implications, *J. Geophys. Res.*, *106*, 29,925–29,933, doi:10.1029/2001JA900120.
Schunk, R., and A. Nagy (2009), *Ionospheres: Physics, Plasma Physics, and Chemistry*, Cambridge Univ. Press, Cambridge, U. K.
Southwood, D. J. (1977), The role of hot plasma in magnetospheric convection, *J. Geophys. Res.*, *82*, 5512–5520, doi:10.1029/JA082i035p05512.
Stonehocker, G. H. (1970), Advanced telecommunication forecasting technique, *AGARD Conf. Proc.*, *49*, 27–1.
Space Weather Prediction Center (2013), Historical SWP products from 1996. [Available at http://www.swpc.noaa.gov/ftpmenu/warehouse.html/.]
Tarpley, J. D. (1970), The ionosphere wind dynamo—I: Lunar tide, *Planet. Space Sci.*, *18*, 1075–1090, doi:10.1016/0032-0633(70)90109-1.
Vasyliunas, V. (1972), *The Interrelationship of Magnetospheric Processes in Earth's Magnetospheric Processes*, Springer, Dordrecht, Netherlands.
Väisälä, V. (1925), Ober die virkung der windeschwankungen auf die pilot beobachtungen, *Comment. Phys. Math.*, *11*, 37.
Vichare, G., A. J. Ridley, and E. Yiğit (2012), Quiet-time low latitude ionospheric electrodynamics in the non-hydrostatic global ionosphere-thermosphere model, *J. Atmos. Sol. Terr. Phys.*, *80*, 161–172, doi:10.1016/j.jastp.2012.01.009.

Wang, W., J. Lei, A. G. Burns, M. Wiltberger, A. D. Richmond, S. C. Solomon, T. L. Killeen, E. R. Talaat, and D. N. Anderson (2008), Ionospheric electric field variations during a geomagnetic storm simulated by a coupled magnetosphere ionosphere thermosphere (CMIT) model, *Geophys. Res. Lett.*, *35*, L18105, doi:10.1029/2008GL035155.

Weimer, D. R. (2005), Improved ionospheric electrodynamic models and application to calculating Joule heating rates, *J. Geophys. Res.*, *110*, A05306, doi:10.1029/2004JA010884.

Yeh, K. C., and C. H. Liu (1974), Acoustic-gravity waves in the upper atmosphere, *Rev. Geophys. Space Phys.*, *12*, 193–216, doi:10.1029/RG012i002p00193.